

The Equilibrium Temperature of Planetary Bodies in Escape Trajectories

Abel Méndez,¹★ Jorge Zuluaga,² Edgard Rivera-Valentín,³ Desiree Cotto-Figueroa⁴

¹*Planetary Habitability Laboratory, University of Puerto Rico at Arecibo, Arecibo, Puerto Rico*

²*Institute of Physics / FCEN - Universidad de Antioquia, Antioquia, Colombia*

³*Lunar and Planetary Institute & Arecibo Observatory, USRA, Texas*

⁴*Department of Physics and Electronics, University of Puerto Rico at Humacao, Humacao, Puerto Rico*

Accepted XXX. Received YYY; in original form ZZZ

ABSTRACT

Many comets, asteroids, and interstellar objects such as 1I/’Oumuamua move in escape trajectories and could experience large but transient variation in temperatures while passing a stellar system. These temperatures are usually calculated by numeric integration over a desired time period. Here we derived analytic solutions for the average equilibrium temperature of any planetary body in escape trajectories, including hyperbolic, parabolic, and linear paths. Our solutions were used to explore the net thermal effect of eccentricity and travel time. We found that 1I/’Oumuamua experienced a mild change in temperature compared to comets in similar trajectories and this probably contributed to the inactivity of any ices in its surface. Thus, interstellar objects in escape trajectories are less likely to exhibit cometary activity from orbital dynamics reasons alone even if ice rich.

Key words: radiation mechanisms: thermal – methods: analytical – comets: general – minor planets, asteroids: individual (1I/2017 U1 ’Oumuamua)

1 INTRODUCTION

The interstellar asteroid 1I/’Oumuamua is the first known extrasolar visitor of our Solar System (Meech et al. 2017a). 1I/’Oumuamua was shown to describe a hyperbolic trajectory consistent with an extrasolar origin (de la Fuente Marcos & de la Fuente Marcos 2017; Wright 2017; Mamajek 2017). Its light curve suggests a tumbling elongated object (3-10:1 ratio) with an effective spherical radius of 102 ± 4 m and little to no cometary activity (Meech et al. 2017b; Knight et al. 2017; Fraser et al. 2017). The source and formation mechanism of 1I/’Oumuamua is still unknown but suggestions include an object ejected from a binary system, among many other alternatives (e.g., Gaidos et al. 2017; Schneider 2017; Zhang 2018; Čuk 2018; Portegies Zwart et al. 2017; Dybczyński & Królikowska 2017; Ferrin & Zuluaga 2017; Zuluaga et al. 2017; Feng & Jones 2017; Do et al. 2018).

The average equilibrium temperature of a planetary body helps to define its general thermal state between the extreme temperatures near periastron and apastron (Méndez & Rivera-Valentín 2017). Bodies in escape trajectories could experience dramatic thermal variations, from the long interstellar environment to transient but strong stellar fluxes

at periastron. This is true for 1I/’Oumuamua and many known comets and asteroids with parabolic and near hyperbolic trajectories in the Solar System (NASA/JPL SSD 2018). Other planetary bodies in highly eccentric elliptical orbits experience similar but periodic wide thermal variations (e.g. comet 1P/Halley).

The surface temperature of small planetary bodies plays a key role in assessing their ice loss rates (Schörghofer & Hsieh 2018). In equilibrium, it is similar to the interior temperature and depends, beside orbital factors, on the albedo, thermal inertia, and the spin axis tilt of the body. The average surface temperature is about 1% lower than the equilibrium temperature for a fast rotator with a zero axis tilt and high thermal inertia, and given by

$$\langle T_s \rangle = \frac{\pi^{1/4}}{5\sqrt{2}} \frac{\Gamma(1/8)}{\Gamma(5/8)} \langle T_{eq} \rangle \approx 0.98882 \langle T_{eq} \rangle \quad (1)$$

where $\langle T_s \rangle$ and $\langle T_{eq} \rangle$ are the global- and time-averaged surface and equilibrium temperatures, respectively (Schörghofer & Hsieh 2018). If the only energy source is from isolation, then it is always the case that $\langle T_s \rangle < \langle T_{eq} \rangle$. For dust covered bodies (i.e., low thermal conductivity), the surface temperature can easily be 20 K lower, which drastically reduces sublimation rates (Schörghofer 2008, 2016).

The rapid change of surface temperatures over a moderately short-time period might produce outgassing of ices

★ E-mail: abel.mendez@upr.edu

Table 1. Representative abundances of ices in comets and their sublimation temperatures T_{sub} in vacuum conditions.

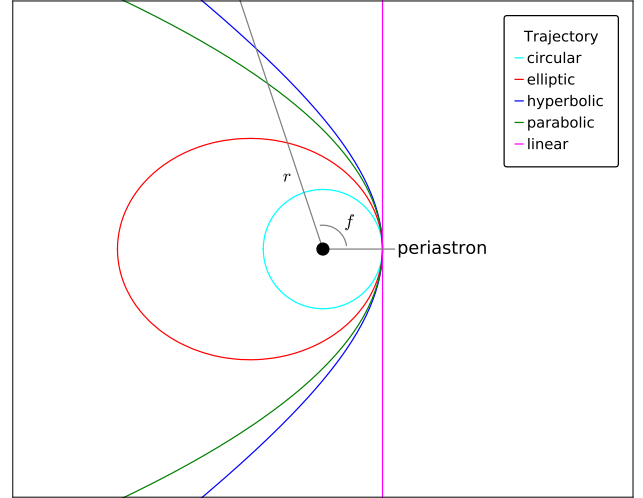
Molecule	Abundance (%) ^a	T_{sub} (K) ^b
H ₂ O	100	144
CO ₂	2 - 30	86
CO	0.4 - 30	28
CH ₄	0.4 - 1.6	36
NH ₃	0.2 - 1.4	102
H ₂ S	0.12 - 1.4	80
HCN	0.1 - 0.25	126
O ₂	-	30

^a Abundances relative to water from Table 3 and 4 of [Mumma & Charnley \(2011\)](#).^b Sublimation temperatures from Table 2 of [Gasc et al. \(2017\)](#).

in planetary bodies, especially comets. For example, ESA’s Rosetta mission monitored a set of eight molecules, including CH₄, NH₃, H₂O, HCN, CO, O₂, H₂S and CO₂, for several weeks post-perihelion, from 2.0 to 3.5 AU, of comet 67P/Churyumov-Gerasimenko ([Gasc et al. 2017](#)). These observations provided a unique opportunity to compare not only the different outgassing patterns of these molecules in a comet, but also their temporal variations as function of illumination. The total outgassing was always dominated by water in the pre-perihelion period ([Fougere et al. 2016](#)). Water seems to follow the sub-solar latitude, which was expected given its rather high sublimation temperature ([Hansen et al. 2016](#)). The general decrease over the period in molecular abundances varies greatly from molecule and it does not follow the sublimation temperatures of pure ices (Table 1).

One of the most important planetary properties to calculate the equilibrium temperature is the bolometric albedo A , also known as the Bond albedo albeit with conflicting definitions in the literature ([Russell 1916](#); [Hanner et al. 1981](#); [Gelino et al. 1999](#); [Mayorga et al. 2016](#)). The bolometric and geometric albedos are related by $A = qA_g$ where A_g is the geometric albedo and q is the phase integral. The bolometric is the albedo as derived by accounting for the full scattering of the surface over all phase angles and wavelengths, while the geometric is the albedo at zero phase angle (*i.e.*, viewing the object directly at opposition along the site of illumination), and can be a function of wavelength. As such, A is always between zero and one and A_g can be higher than one, depending on the scattering properties normalized to an ideal surface (*e.g.* for Enceladus $A = 0.8$ and $A_g = 1.4$).

Because A requires more information to calculate a significant q , it is not easy to relate to A_g . For example, the spherical albedo A_s for an ideal Lambertian surface at a specific wavelength is related to the geometric albedo by $A_s = \frac{3}{2}A_g$, but this assumption overestimates A ([Dyudina et al. 2016](#)). When possible, the A should be calculate as a function of latitude and longitude for a given shape model because it also dependent on the scattering properties and topography of the body. Alternatively, a spherical bolometric albedo can be calculated as a gross body wide value. For asteroids and comets this is a rough approximation because it assumes a spherical shape, and they are rarely spheres.

**Figure 1.** Comparison of escape trajectories with those of circular and elliptical orbits with a common periastron.

Nevertheless, it is possible to estimate approximate spherical bolometric albedos for asteroids from their visual geometric albedos using the empirical relation

$$A = (0.290 + 0.684G)A_g \quad (2)$$

where the slope parameter G describes the change in the brightness of the object at different illumination phase angles ([Schläppi et al. 2008](#)). A mean value of $G = 0.18 \pm 0.13$ could be used for asteroids based on observational data from the JPL Small-Bodies Database ([Cotto-Figueroa 2013](#)). Thus, the average bolometric albedos for asteroids can be estimated from equation 2 and their distribution of geometric albedos (Table 2). [Usui et al. \(2013\)](#) calculated geometric albedos for 5120 asteroids measured by the infrared astronomical satellite AKARI. See for example [Bowell et al. \(1989\)](#), [Shestopalov & Golubeva \(2011\)](#), [Li et al. \(2013\)](#) or [Delbo et al. \(2015\)](#) for more details on the calculation of bolometric albedos of asteroids from photometric data.

The goal of our study is to compare the thermal state between planetary bodies in closed and open trajectories. We derive analytic solutions for the temporal average of orbital distance, stellar flux, and equilibrium temperature of planetary bodies in escape trajectories. They were derived by integration with respect to time as described in [Méndez & Rivera-Valentín \(2017\)](#) for elliptical orbits. Our solutions were also compared with circular and elliptical orbits as defined in Table A1 and shown in Figure 1.

Section 2 describes solutions of elliptical orbits for comparison purposes. Sections 3, 4, and 5 present our new derivations for parabolic, hyperbolic, and linear trajectories, respectively. Section 6 discuss the validation of our results with numerical simulations and applications to Solar System and extrasolar planetary bodies, including I1/Oumuamua.

2 ELLIPTICAL ORBITS

Temporal averages for orbital distance $\langle r \rangle$, stellar flux $\langle F \rangle$, and equilibrium temperature $\langle T_{eq} \rangle$ for elliptic orbits were

Table 2. General properties of S, X, and C type asteroids.^a

Spectral Type	Abundance (%)	Density (gcm ⁻³)	A _g
S	62	2.660 ± 0.594	0.26 ± 0.035
X	22	2.819 ± 0.631	0.31 ± 0.075
C	16	1.626 ± 0.568	0.13 ± 0.055

^a Adapted from Cotto-Figueroa (2013).

derived by Méndez & Rivera-Valentín (2017). They were solved by calculating the average value integrating over time t around the orbital period T and making the substitutions $r = a(1 - e \cos E)$, $M = E - e \sin E$, and $M = (2\pi/T)t$; where r is position, e is the orbital eccentricity, a is the semi-major axis in astronomical units, E is the eccentric anomaly, and M is the mean anomaly. These averages are

$$\langle r \rangle = a \left(1 + \frac{e^2}{2} \right), \quad (3)$$

$$\langle F \rangle = \frac{L}{a^2 \sqrt{1 - e^2}}, \quad (4)$$

$$\langle T_{eq} \rangle = T_o \left[\frac{(1 - A)L}{\beta \epsilon a^2} \right]^{\frac{1}{4}} \frac{2\sqrt{1 + e}}{\pi} \mathbf{E} \left(\frac{2e}{1 + e} \right), \quad (5)$$

where L is the stellar luminosity in solar units, A the bond albedo, ϵ the emissivity, β the redistribution factor, $T_o = 278.5$ K, and \mathbf{E} is the complete elliptic integral of the second kind (Weisstein 2016; GSL 2016). The definition of $\mathbf{E}(2e/(1 + e))$ used in equation 5 is the one implemented in software packages like *Mathematica* (i.e., `EllipticE`) and *Maxima* (i.e., `elliptic_ce`). The *GNU Scientific Library* (GSL) uses `gsl_sf_ellint_Ecomp` which requires first the square root of the argument (i.e., $\mathbf{E}(\sqrt{2e/(1 + e)})$).

For elliptical orbits the average distance ($a \leq \langle r \rangle < \frac{3}{2}a$) and stellar flux ($F|_{e=0} \leq \langle F \rangle < \infty$) increase with eccentricity. However, the average equilibrium temperature ($T_{eq}|_{e=0} \leq \langle T_{eq} \rangle < \frac{2\sqrt{2}}{\pi} T_{eq}|_{e=0}$) slowly decreases with eccentricity until converging to $\sim 90\%$ of the equilibrium temperature for circular orbits (Figure 2). Table 3 shows these averages calculated for some minor planetary bodies with highly eccentric orbits. Note that the $\langle T_{eq} \rangle$ of comet 1P/Halley is about 70 K and not 92 K from the commonly assumed but incorrect expression $\langle T_{eq} \rangle = T_o[\langle F \rangle(1 - A)]^{\frac{1}{4}}$.

Equations 3 to 5 are averages for a full orbital period, but to compare with escape trajectories we also derived expressions for the path near periastron $E = 0$ between the eccentric anomalies $-E_o$ to $+E_o$. From the integration over time we obtained

$$\langle r \rangle = a \left[\frac{(e^2 + 2)E_o + e(e \cos E_o - 4) \sin E_o}{2(E_o - e \sin E_o)} \right], \quad (6)$$

$$\langle F \rangle = \frac{L}{a^2} \left[\frac{2 \tan^{-1} \left(\sqrt{\frac{1+e}{1-e}} \tan \frac{1}{2} E_o \right)}{(E_o - e \sin E_o) \sqrt{1 - e^2}} \right], \quad (7)$$

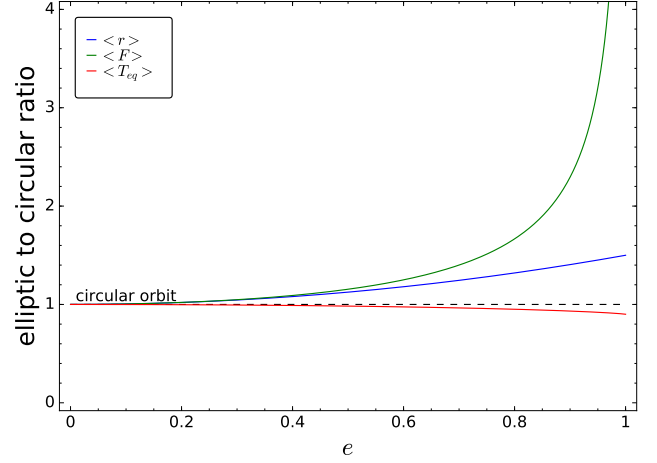


Figure 2. Comparison of temporal averages of orbital distance, stellar flux, and equilibrium temperature as a function of eccentricity e for elliptical orbits with constant semi-major axis (normalized with respect to circular orbits).

$$\langle T_{eq} \rangle = T_o \left[\frac{L(1 - A)}{a^2} \right]^{\frac{1}{4}} \frac{2i \sqrt{1 - e}}{E_o - e \sin E_o} \dots \left(\mathbf{E}(q|p) - \mathbf{F}(q|p) - i \sqrt{\frac{1 - e \cos E_o}{1 - e}} \tan \frac{1}{2} E_o \right) \quad (8)$$

where $q = i \sinh^{-1}(\tan \frac{1}{2} E_o)$, $p = (1 + e)/(1 - e)$, \mathbf{E} is the incomplete elliptic integral of the second kind, and \mathbf{F} is the incomplete elliptic integral of the first kind.

3 PARABOLIC TRAJECTORIES

Planetary bodies with speeds near the escape velocity around a star move in parabolic paths. We integrated the averages for parabolic trajectories taking $r = r_p(1 + D^2)$, $M = D + \frac{1}{3}D^3$, and $M = (2M_o/T)t - M_o$; where D is the parabolic anomaly from $-D_o$ to $+D_o$. They are given by

$$\langle r \rangle = r_p \left[\frac{3D_o^4 + 10D_o^2 + 15}{5(D_o^2 + 3)} \right], \quad (9)$$

$$\langle F \rangle = \frac{L}{r_p^2} \left[\frac{3 \tan^{-1} D_o}{(D_o^2 + 3) D_o} \right], \quad (10)$$

Table 3. Temporal averages of orbital distance $\langle r \rangle$, stellar flux $\langle F \rangle$, and equilibrium temperature $\langle T_{eq} \rangle$ for some planetary bodies with eccentric orbits ($e > 0.2$) including comets, asteroids, Trans-Neptunian Objects (TNO), and planets.

Object Description ^a						Temporal Averages ^d		
Name	Type	a (AU)	e	A_g ^b	A^c	$\langle r \rangle$ (AU)	$\langle F \rangle$	$\langle T_{eq} \rangle$ (K)
1P/Halley	HTC	17.834145	0.96714291	0.04	0.02	26.174	0.0123	60.0
2P/Encke	JFC	2.2151323	0.84832024	0.046	0.02	3.0122	0.384	176
9P/Tempel 1	JFC	3.1457942	0.50964598	0.056	0.013	3.5543	0.117	154
67P/Churyumov-Gerasimenko	JFC	3.4647374	0.64058232	0.06	0.03	4.1756	0.108	144
81P/Wild 2	JFC	3.4518811	0.53707199	0.063	0.012	3.9497	0.0994	147
103P/Hartley 2	JFC	3.4725219	0.69512663	0.045	0.012	4.3114	0.115	144
253 Mathilde	C	2.6506802	0.26320066	0.041	0.013	2.7424	0.148	170
433 Eros	S	1.45794	0.22258897	0.23	0.092	1.4941	0.483	224
1566 Icarus	S	1.0779459	0.8268093	0.29	0.08	1.4464	1.53	249
9969 Braille	Q	2.3410243	0.43344223	0.34	0.14	2.5609	0.204	173
25143 Itokawa	S	1.3241134	0.28016847	0.33	0.14	1.3760	0.594	232
101955 Bennu	B	1.126391	0.20374511	0.047	0.016	1.1498	0.805	261
90377 Sedna	SD?	487.7651	0.8440912	0.32	0.19	661.53	7.84×10^{-6}	11.3
90482 Orcus	KBO	39.3976243	0.22008902	0.28	0.15	40.352	6.60×10^{-4}	42.5
134340 Pluto	KBO	39.4450697	0.25024871	0.62	0.72	40.680	6.64×10^{-4}	32.1
136199 Eris	SD	67.6487798	0.44172397	0.96	0.55	74.249	2.44×10^{-4}	27.4
225088 2007 OR ₁₀	SD	67.1436607	0.50577423	0.089	0.06	75.731	2.57×10^{-4}	32.9
Mercury	Planet	0.38709927	0.20563593	0.106	0.088	0.3953	6.82	436

^a Object elements from the NASA Solar System Dynamic website https://ssd.jpl.nasa.gov/?sb_elem.^b Geometric albedos from Lamy et al. (2004); Brown et al. (2010); Sicardy et al. (2011); Pál et al. (2012); Nugent et al. (2015); Capaccioni et al. (2015); Takir et al. (2015); Pál et al. (2016), and Table 6 of Li et al. (2013).^c Bond albedos from Campins et al. (1981); Hartmann et al. (1987); Buratti et al. (2004); Brown et al. (2010); Sicardy et al. (2011); Takir et al. (2015); Mallama (2017); Buratti et al. (2017), Table 6 of Li et al. (2013), and Table 1 of Johnson et al. (2015). Value for 1566 Icarus assuming the average for S-type asteroids. Value for 90482 Orcus assuming a phase integral of $q \approx 0.55$, similar to the icy satellites of Uranus.^d Average values calculated with equations 3, 4, and 5, respectively. Equilibrium temperatures assuming a fast rotator ($\beta=1$) with unit emissivity ($\epsilon=1$).

$$\langle T_{eq} \rangle = T_o \left[\frac{L(1-A)}{\beta \epsilon r_p^2} \right]^{\frac{1}{4}} \left[\frac{3(D_o \sqrt{D_o^2 + 1} + \sinh^{-1} D_o)}{2(D_o^2 + 3)D_o} \right]. \quad (11)$$

The average distance ($r_p \leq \langle r \rangle < \infty$) increase with orbital time (*i.e.* large D_o) to infinity as expected for open orbits such as a parabolic trajectories. Accordingly, the average stellar flux ($F(r_p) \leq \langle F \rangle < 0$) and equilibrium temperature ($T_{eq}(r_p) \leq \langle T_{eq} \rangle < 0$) decreases with time to zero.

4 HYPERBOLIC TRAJECTORIES

Planetary bodies with speeds over the escape velocity around a star move in hyperbolic paths. The period of integration T was taken from entering to leaving the stellar system where the time to periastron is the semi-period $\frac{1}{2}T$. The integrals were solved by making the substitutions $r = r_p(1 - e \cosh H)/(1 - e)$, $M = e \sinh H - H$, and $M = (2M_o/T) - M_o$; where r_p is the periastron, H is the hyperbolic eccentricity and the objects move between time zero to T , corresponding to $-M_o$ to $+M_o$ in the mean anomaly and $-H_o$ to $+H_o$ in the hyperbolic anomaly. The distance, stellar flux, and equilibrium temperature averages are then

given with respect to the hyperbolic anomaly as

$$\langle r \rangle = r_p \left[\frac{e(e \cosh H_o - 4) \sinh H_o + (e^2 + 2)H_o}{2(e \sinh H_o - H_o)(e - 1)} \right], \quad (12)$$

$$\langle F \rangle = \frac{L}{r_p^2} \left[\frac{2(e-1)^2(e^2-1)^{-\frac{1}{2}}}{e \sinh H_o - H_o} \tan^{-1} \left(\frac{(e+1) \tanh \frac{1}{2} H_o}{\sqrt{e^2-1}} \right) \right], \quad (13)$$

$$\langle T_{eq} \rangle = T_o \left[\frac{L(1-A)}{\beta \epsilon r_p^2} \right]^{\frac{1}{4}} \left[\frac{-2i(e-1)}{e \sinh H_o - H_o} \mathbf{E} \left(\frac{1}{2} i H_o \mid \frac{2e}{e-1} \right) \right] \quad (14)$$

where \mathbf{E} is the incomplete elliptic integral of the second kind (Weisstein 2016; GSL 2016). As in equation 5, the definition of \mathbf{E} used in equation 14 is the one implemented in *Mathematica* or *Maxima* and not in GSL. Note that equation 14 also involves operations with imaginary numbers.

For hyperbolic trajectories the average distance ($r_p \leq \langle r \rangle < \infty$) increase with orbital time (*i.e.* large H_o) to infinity, but decreases with eccentricity. The average stellar flux ($F(r_p) \leq \langle F \rangle < 0$) and equilibrium temperature ($T_{eq}(r_p) \leq \langle T_{eq} \rangle < 0$) decreases with time to zero, but the

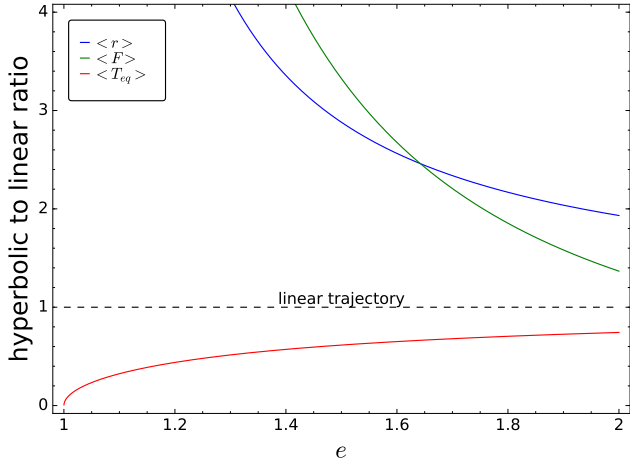


Figure 3. Comparison of temporal averages of orbital distance, stellar flux, and equilibrium temperature as a function of eccentricity e for hyperbolic trajectories with constant periastron (normalized with respect to linear trajectories). Hyperbolic trajectories converge to linear trajectories for $e \rightarrow \infty$.

flux decreases with eccentricity while the temperature increases. All these averages converge to those of a linear trajectory (Section 5) for large eccentricities (Figure 3).

5 LINEAR TRAJECTORIES

Planetary bodies that are moving fast and far from a star could move in near-linear paths. These trajectories are a special case of the hyperbolic trajectories where e equal to infinity. We solved equations 12 to 14 for $\lim_{e \rightarrow \infty}$ obtaining

$$\langle r \rangle = r_p \left[\frac{\sinh 2H_o + 2H_o}{4 \sinh H_o} \right], \quad (15)$$

$$\langle F \rangle = \frac{L}{r_p^2} \left[\frac{2 \tan^{-1} \left(\tanh \frac{1}{2} H_o \right)}{\sinh H_o} \right], \quad (16)$$

$$\langle T_{eq} \rangle = T_o \left[\frac{L(1-A)}{\beta \epsilon r_p^2} \right]^{\frac{1}{4}} \left[\frac{-2i}{\sinh H_o} \mathbf{E} \left(\frac{1}{2} i H_o \middle| 2 \right) \right]. \quad (17)$$

For linear trajectories the average distance ($r_p \leq \langle r \rangle < \infty$) increase with orbital time (*i.e.* large H_o) to infinity. The average stellar flux ($F(r_p) \leq \langle F \rangle < 0$) and equilibrium temperature ($T_{eq}(r_p) \leq \langle T_{eq} \rangle < 0$) decreases with time to zero.

6 DISCUSSION

Our analytic solutions for the average distance, stellar flux, and equilibrium temperature of planetary bodies in elliptic, parabolic, hyperbolic, and linear trajectories (Equations 3 to 17) were validated with numerical solutions. We performed numerical integrations of the average function with respect to time in IDL using the fourth-order Runge-Kutta procedure RK4. Both the analytic expressions and numerical solutions agreed in all cases. We also verified our solutions with

a boundary-value analysis with respect to eccentricity and conic anomalies (*i.e.*, the elliptical, parabolic, and hyperbolic anomalies). The perihelion elliptic solutions (equations 6 to 8) converge to the full orbit elliptic solutions (equations 3 to 5) for $E_o = \pi$. The hyperbolic solutions (equations 12 to 14) converge to the linear solutions (equations 15 to 17) for $e \rightarrow \infty$.

Our solutions assume that the albedo remains constant during the trajectory. This might be true for airless bodies such as asteroids but not necessarily for comets, especially near perihelion and after the formation of the coma. For instance, dust from the coma might increase the total sunlight reaching the nucleus. The coma provides an isotropic source of scattered sunlight and thermal emission over the entire nucleus surface due to its significantly greater geometrical cross section as compared with the nucleus (Weissman & Kieffer 1981). Also, significant mass losses could expose materials with different ice/dirt ratios and hence different thermal or optical properties (Hartmann & Cruikshank 1984). All these processes are a strong function of heliocentric distance and more significant for near-Sun comets (*i.e.*, $r_p < 0.307$ AU) (Jones et al. 2018). However, we are assuming here that heliocentric variations in the bolometric albedo are negligible for simplicity.

The averages for escape trajectories become $\langle r \rangle = \infty$, $\langle F \rangle = 0$, and $\langle T_{eq} \rangle = 0$ for large times. Thus, they are meaningless unless they are calculated with respect to some fixed boundaries. One alternative is to calculate these averages after some heliocentric distance when the planetary body is considered under the influence of the Solar System (*e.g.* within the heliopause ~ 122 AU, Cairns & Fuselier (2017)). Other alternative is to use some standard time of comparison around periastron (*e.g.* one year). Another alternative is to calculate averages after the body is above some critical temperature (*e.g.* 170 K snow line, Kennedy & Kenyon (2008)).

One way to compare hyperbolic trajectories with elliptic orbits is under the same time frame. This could be the orbital period of the elliptic orbit but with the same periastron of the hyperbolic trajectory (periods shown in Table A1). We calculated the ratio between the average equilibrium temperature of hyperbolic trajectories $\langle T_{eq} \rangle_H$ and that of elliptic orbits $\langle T_{eq} \rangle_E$ for the same periastron and period (Figure 4). The temperatures for hyperbolic orbits are always less than that of the equivalent elliptic orbits for any combination of the elliptic and hyperbolic eccentricities. Temperatures also decrease with the hyperbolic eccentricity. This trend is also true for parabolic and linear trajectories. Therefore, planetary objects in escape trajectories always experience lower temperatures than those in equivalent elliptical orbits (*i.e.* same period and periastron).

Probably the best way to compare the average equilibrium temperature of planetary objects in both closed or open orbits is after some critical temperature. One alternative is between the time that the surface temperatures of the object reach the sublimation temperature of a major component, such as water or carbon dioxide (Table 1). Average surface temperatures are similar to the equilibrium temperature as shown in equation 1.

Table 4 shows these properties calculated for some minor planetary bodies in escape trajectories such as 1I/Oumuamua.

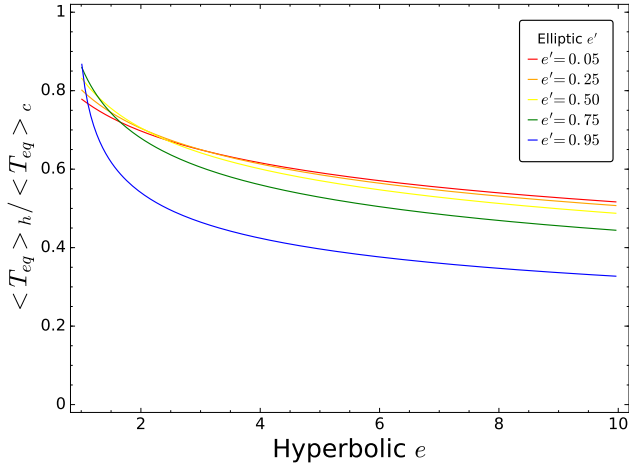


Figure 4. Ratio of the average equilibrium temperature between hyperbolic trajectory and equivalent elliptic orbits with the same periastron and period (periastron time for the hyperbolic trajectory). The average temperature for hyperbolic trajectories is always less than that of an equivalent elliptic orbit.

In the case of 1I/'Oumuamua, it is not spherical and there is not enough photometric information over a wide range of wavelengths and phase angles to confidently calculate its bolometric albedo. However, we can just do a thermal study looking at potential A values, from comet to asteroid.

Relevance to visiting rogue exoplanets, if any. (e.g. expected comet-like tails, atmospheric erosion. Relevance to interstellar travel. Recharge batteries from stellar flybys. Implications to panspermia.

7 CONCLUSION

We derived analytic expressions for the average distance, stellar flux, and equilibrium temperature of planetary bodies in hyperbolic, parabolic, and linear trajectories. Our expressions were validated with numerical solutions and applied to asteroids and comets. We found that the average equilibrium temperature of bodies in escape trajectories with constant periastron increase with eccentricity until they converge to the values for linear trajectories. We suggest that the best way to compare the thermal state between planetary bodies in elliptic and escape trajectories is within the snow line, near periastron.

Our analysis on 1I/'Oumuamua shows that its average temperature within XXX region was XXX K and not high enough for a significant sublimation of any surface ices. We suggest that this low temperature and an organic crust as proposed by Fitzsimmons et al. (2017) were probably responsible for its lack of cometary activity.

ACKNOWLEDGEMENTS

This work was supported by the Planetary Habitability Laboratory (PHL) of the University of Puerto Rico at Arecibo (UPR Arecibo). We would like to thank Guillermo Nery for helpful suggestions.

REFERENCES

- Bowell, E., Hapke, B., Domingue, D., et al. 1989, *Asteroids II*, 524
- Brown, M. E., Ragozzine, D., Stansberry, J., & Fraser, W. C. 2010, *AJ*, 139, 2700
- Buratti, B. J., Britt, D. T., Soderblom, L. A., et al. 2004, *Icarus*, 167, 129
- Buratti, B. J., Hofgartner, J. D., Hicks, M. D., et al. 2017, *Icarus*, 287, 207
- Cairns, I. H., & Fuselier, S. A. 2017, *ApJ*, 834, 197
- Campins, H., Gradie, J., Lebofsky, M., & Rieke, G. 1981, *Modern Observational Techniques for Comets*, 347, aaa0628
- Capaccioni, F., Coradini, A., Filacchione, G., et al. 2015, *Science*, 347, aaa0628
- Cotto-Figueroa, D. 2013, Ph.D. Thesis,
- Ćuk, M. 2018, *ApJ*, 852, L15
- de la Fuente Marcos, C., & de la Fuente Marcos, R. 2017, *Research Notes of the American Astronomical Society*, 1, 5
- Delbo, M., Mueller, M., Emery, J. P., Rozitis, B., & Capria, M. T. 2015, *Asteroids IV*, 107
- Do, A., Tucker, M. A., & Tonry, J. 2018, arXiv:1801.02821
- Dybczyński, P. A., & Królikowska, M. 2017, arXiv:1711.06618
- Dyudina, U., Zhang, X., Li, L., et al. 2016, *ApJ*, 822, 76
- Feng, F., & Jones, H. R. A. 2017, arXiv:1711.08800
- Ferrin, I., & Zuluaga, J. 2017, arXiv:1711.07535
- Fitzsimmons, A., Snodgrass, C., Rozitis, B., et al. 2017, arXiv:1712.06552
- Fraser, W. C., Pravec, P., Fitzsimmons, A., et al. 2017, *Nature Astronomy*, 1,
- Fougere, N., Altwegg, K., Berthelier, J.-J., et al. 2016, *MNRAS*, 462, S156
- Gaidos, E., Williams, J., & Kraus, A. 2017, *Research Notes of the American Astronomical Society*, 1, 13
- Gasc, S., Altwegg, K., Balsiger, H., et al. 2017, *MNRAS*, 469, S108
- Gelino, C. R., Marley, M., Stephens, D., Lunine, J., & Freedman, R. 1999, *Physics and Chemistry of the Earth C*, 24, 573
- GNU Scientific Library 2016, *Legendre Form of Complete Elliptic Integrals*. From the GNU Scientific Library. <http://www.gnu.org/software/gsl>
- Hanner, M. S., Giese, R. H., Weiss, K., & Zerull, R. 1981, *A&A*, 104, 42
- Hansen, K. C., Altwegg, K., Berthelier, J.-J., et al. 2016, *MNRAS*, 462, S491
- Hartmann, W. K., & Cruikshank, D. P. 1984, *Icarus*, 57, 55
- Hartmann, W. K., Tholen, D. J., & Cruikshank, D. P. 1987, *Icarus*, 69, 33
- Johnson, R. E., Oza, A., Young, L. A., Volkov, A. N., & Schmidt, C. 2015, *ApJ*, 809, 43
- Jones, G. H., Knight, M. M., Battams, K., et al. 2018, *Space Sci. Rev.*, 214, #20
- Kennedy, G. M., & Kenyon, S. J. 2008, *ApJ*, 673, 502-512
- Knight, M. M., Protapapa, S., Kelley, M. S. P., et al. 2017, *ApJ*, 851, L31
- Lamy, P. L., Toth, I., Fernandez, Y. R., & Weaver, H. A. 2004, *Comets II*, 223
- Li, J.-Y., Le Corre, L., Schröder, S. E., et al. 2013, *Icarus*, 226, 1252
- Mallama, A. 2017, arXiv:1703.02670
- Mamajek, E. 2017, *Research Notes of the American Astronomical Society*, 1, 21
- Mayorga, L. C., Jackiewicz, J., Rages, K., et al. 2016, *AJ*, 152, 209
- Meech, K., Bacci, P., Mastrapieri, M., et al. 2017, *Minor Planet Electronic Circulars*, 2017-U183
- Meech K. J., et al., 2017, *Nature*, 552, 378
- Méndez, A., & Rivera-Valentín, E. G. 2017, *ApJ*, 837, L1

Table 4. Temporal averages of orbital distance $\langle r \rangle$, stellar flux $\langle F \rangle$, and equilibrium temperature $\langle T_{eq} \rangle$ within the snow line for 'Oumuamua and some comets with similar perihelion. 1I/'Oumuamua experienced slightly higher temperatures but in a much shorter period.

Name	Orbital Parameters ^a		Period and Temporal Averages for $T > 170$ K ^b			
	r_p (AU)	e	P (yrs)	$\langle r \rangle$ (AU)	$\langle F \rangle$	$\langle T_{eq} \rangle$ (K)
1I/'Oumuamua	0.25534	1.19951	0.571	1.4813	1.70	261
C/1901 G1 (Great Comet)	0.244812	1	1.01	1.5419	1.57	254
C/1905 X1 (Giacobini)	0.2159002	1	1.01	1.5440	1.71	255
C/1948 L1 (Honda-Bernasconi)	0.207628	0.999875	0.722	1.5448	1.76	255
C/1975 V2 (Bradfield)	0.21872078	1.00001667	0.725	1.5437	1.70	255
C/1980 Y1 (Bradfield)	0.259823	0.999725	0.739	1.5413	1.50	253
C/1984 N1 (Austin)	0.291284	0.999846	0.748	1.5405	1.38	252
C/1996 B2 (Hyakutake)	0.23022931	0.99989867	0.729	1.5429	1.64	255

^a Object elements from the NASA Solar System Dynamic website https://ssd.jpl.nasa.gov/?sb_elem.

^b Average values calculated for elliptic, parabolic and hyperbolic trajectories (equations 9 to 14) and using a comet-like albedo of 0.02 for comparison purposes.

- Mumma, M. J., & Charnley, S. B. 2011, ARA&A, 49, 471
 NASA/JPL Solar System Dynamics. <https://ssd.jpl.nasa.gov/>
 Nugent, C. R., Mainzer, A., Masiero, J., et al. 2015, ApJ, 814, 117
 Pál, A., Kiss, C., Müller, T. G., et al. 2012, A&A, 541, L6
 Pál, A., Kiss, C., Müller, T. G., et al. 2016, AJ, 151, 117
 Portegies Zwart, S., Pelupessy, I., Bedorf, J., Cai, M., & Torres, S. 2017, arXiv:1711.03558
 Russell, H. N. 1916, Proceedings of the National Academy of Science, 2, 74
 Sicardy, B., Ortiz, J. L., Assafin, M., et al. 2011, Nature, 478, 493
 Schläppi, B., Altwegg, K., & Wurz, P. 2008, Icarus, 195, 674
 Schneider, J. 2017, Research Notes of the American Astronomical Society, 1, 18
 Schorghofer, N. 2008, ApJ, 682, 697-705
 Schorghofer, N. 2016, Icarus, 276, 88
 Schörghofer, N., & Hsieh, H. H. 2018, arXiv:1802.01293
 Shestopalov, D. I., & Golubeva, L. F. 2011, Lunar and Planetary Science Conference, 42, 1028
 Takir, D., Clark, B. E., Drouet d'Aubigny, C., et al. 2015, Icarus, 252, 393
 Usui, F., Kasuga, T., Hasegawa, S., et al. 2013, ApJ, 762, 56
 Weissman, P. R., & Kieffer, H. H. 1981, Icarus, 47, 302
 Weisstein, Eric W. 2016, Complete Elliptic Integral of the Second Kind. From MathWorld—A Wolfram Web Resource. <http://mathworld.wolfram.com>
 Wright, J. T. 2017, Research Notes of the American Astronomical Society, 1, 38
 Zhang, Q. 2018, ApJ, 852, L13
 Zuluaga, J. I., Sanchez-Hernandez, O., Sucerquia, M., & Ferrin, I. 2017, arXiv:1711.09397

APPENDIX A: ORBITAL ELEMENTS

This paper has been typeset from a $\text{\TeX}/\text{\LaTeX}$ file prepared by the author.

Table A1. Orbital elements of circular, elliptic, parabolic, hyperbolic, and linear trajectories. Only the linear trajectory is an impossible path.

Orbital Element	Circular $e = 0$	Elliptic $0 < e < 1$	Parabolic $e = 1$	Hyperbolic ^a $1 < e < \infty$	Linear $e = \infty$
Position, $r(f)$	$r = a$	$r = \frac{a(1-e^2)}{1+e \cos f}$	$r = r_p \frac{2}{1+\cos f}$	$r = r_p \frac{1+e}{1+e \cos f}$	$r = r_p \csc f$
Position, $r(E, D, \text{ or } H)$	$r = a$	$r = a(1 - e \cos E)$	$r = r_p(1 + D^2)$	$r = r_p \frac{e \cosh H - 1}{e - 1}$	$r = r_p \cosh H$
Periastron, r_p	$r_p = a$	$r_p = a(1 - e)$	$r_p = r_p$	$r_p = r_p$	$r_p = r_p$
Apastron, r_a	$r_a = a$	$r_a = a(1 + e)$	$r_a = \infty$	$r_a = \infty$	$r_a = \infty$
True Anomaly, f	$f = E$	$\tan \frac{f}{2} = \sqrt{\frac{e+1}{e-1}} \tan \frac{E}{2}$	$\tan \frac{f}{2} = D$	$\tan \frac{f}{2} = \sqrt{\frac{e+1}{e-1}} \tanh \frac{H}{2}$	$\tan \frac{f}{2} = \tanh \frac{H}{2}$
Conic Anomaly, $E, D, \text{ or } H$	$E = f$	$\cos E = \frac{e + \cos f}{1 + e \cos f}$	$D = \tan \frac{f}{2}$	$\tanh \frac{H}{2} = \sqrt{\frac{e-1}{e+1}} \tanh \frac{f}{2}$	$\tanh \frac{H}{2} = \tanh \frac{f}{2}$
Mean Anomaly, M	$M = E$	$M = E - e \sin E$	$M = D + \frac{1}{3}D^3$	$M = e \sinh H - H$	undefined
Time from Periastron, t	$t = M \sqrt{\frac{a^3}{\mu}} + t_o$	$t = M \sqrt{\frac{a^3}{\mu}} + t_o$	$t = M \sqrt{\frac{2r_p^3}{\mu}} + t_o$	$t = M \sqrt{\frac{r_p^3}{\mu(e-1)^3}} + t_o$	undefined
Period, P	$P = 2\pi \sqrt{\frac{a^3}{\mu}}$	$P = 2\pi \sqrt{\frac{a^3}{\mu}}$	$P = 2M_o \sqrt{\frac{2r_p^3}{\mu}}$	$P = 2M_o \sqrt{\frac{r_p^3}{\mu(e-1)^3}}$	undefined
True Anomaly Range	$0 \leq f \leq 2\pi$	$0 \leq f \leq 2\pi$	$-\pi < f < +\pi$	$-\cos^{-1}(-\frac{1}{e}) < f < +\cos^{-1}(-\frac{1}{e})$	$-\frac{\pi}{2} < f < +\frac{\pi}{2}$
Conic Anomaly Range	$0 \leq E \leq 2\pi$	$0 \leq E \leq 2\pi$	$-\infty < D < +\infty$	$-\infty < H < +\infty$	$-\infty < H < +\infty$
Mean Anomaly Range	$0 \leq M \leq 2\pi$	$0 \leq M \leq 2\pi$	$-\infty < M < +\infty$	$-\infty < M < +\infty$	undefined

^a Hyperbolic equations are expressed in terms of the periastron instead of semi-major axis.